Supplemental Material - Microscopic origin of the mobility enhancement at a spinel/perovskite oxide heterointerface revealed by photoemission spectroscopy

P. Schütz,[1] D.V. Christensen,[2] V. Borisov,[3] F. Pfaff,[1] P. Scheiderer,[1] L. Dudy,[1] M. Zapf,[1] J. Gabel,[1] Y.Z. Chen,[2] N. Pryds,[2] V.A. Rogalev,[4,1] V.N. Strocov,[4] C. Schlueter,[5] T.-L. Lee,[5] H.O. Jeschke,[3] R. Valentí,[3] M. Sing,[1] and R. Claessen[1]

[1] *Physikalisches Institut and Röntgen Center for Complex Material Systems (RCCM), Universität Würzburg, Am Hubland, D-97074 Würzburg, Germany*

[2] *Department of Energy Conversion and Storage, Technical University of Denmark, 4000 Roskilde, Denmark*

[3] *Institute of Theoretical Physics, Goethe University Frankfurt am Main, D-60438 Frankfurt am Main, Germany*

[4] *Swiss Light Source, Paul Scherrer Institut, CH-5232 Villigen, Switzerland*

[5] *Diamond Light Source, Harwell Sciene and Innovation Campus, Oxfordshire OX11 0DE, United Kingdom*

(Dated: August 11, 2017)

SUPPLEMENTAL MATERIAL I. EXPERIMENTAL DETAILS

A. Spectroscopy experiments

The experiments were performed at the combined soft and hard x-ray beamline I09 at the Diamond Light Source and the soft x-ray beamline ADRESS at the Swiss Light Source.[1,2] At I09 a SCIENTA EW4000 photoelectron spectrometer with parallel angular detection range of 60° is used in combination with a 5-axis manipulator. Data were acquired at a sample temperature of 50 K and an overall energy resolution of 80 meV. In-situ dosing with high-purity oxygen was accomplished through a metal capillary pointed at the sample.

At ADRESS a SPECS PHOIBOS-150 photoelectron analyzer is used in combination with a 6-axis CARVING manipulator. Here, oxygen dosing experiments were performed by flooding the analyzer chamber with oxygen. Data were acquired at a sample temperature of 10 K and an overall energy resolution of 80 meV.

All samples were grounded with silver paint to prevent charging. Significant intensity from the Ti $2p$ core level excited by second order light from the undulator appeared in all spectra in the region around the chemical potential. If not stated otherwise, all spectra are corrected for and normalized to this component.

B. Sample fabrication

$LaAlO_3/SrTiO_3$ heterostructures were grown by pulsed laser deposition (PLD) on TiO_2-terminated $SrTiO_3$ substrates in Würzburg as described in Ref. [3]. The oxygen background pressure amounted to 1×10^{-4} mbar while the substrate was kept at 780°C. Subsequently, a post-growth oxidation step was performed at 500 mbar oxygen pressure during cool-down to suppress oxygen vacancies in the $SrTiO_3$ bulk. The γ-$Al_2O_3/SrTiO_3$ heterostructures were PLD-grown at DTU Energy, Denmark, as described in Ref. [4] and [5]. The shown data were obtained for a film thickness of 2.25 unit cells of γ-Al_2O_3 ($\approx$ 18 Å) but have been reproduced for several film thicknesses. In addition to the original report[4], the high mobility γ-$Al_2O_3/SrTiO_3$ heterostructures were reproduced in another PLD chamber after a careful optimization of the deposition parameters. Here, the films were grown at 650°C and an oxygen pressure of 1×10^{-5} mbar rather than 600°C 1×10^{-4} mbar. Prior to the photoemission spectroscopy experiments they exhibited a Hall mobility of $80,000\,\mathrm{cm^2/Vs^{-1}}$ at 4 K. Note that the γ-$Al_2O_3/SrTiO_3$ samples have not been exposed to a post-growth oxidation procedure since this will quench conductivity,[4] thus indicating the importance of oxygen vacancy doping in these samples.

SUPPLEMENTAL MATERIAL II. IN-GAP Ti 3*d* PHOTON ENERGY DEPENDENCE AT FIXED OXYGEN STOICHIOMETRY

Complementary to Fig. 2(a) (main paper), the Ti 3*d* spectral weight was measured as function of photon energy at the maximum and minimum (no) oxygen dosing. Figure S1 depicts the photon energy dependence, selected spectra normalized to the in-gap spectral weight, and the resulting constant initial state (CIS) spectra of the relevant spectral features. For maximum dosing, it becomes apparent that in-gap feature B (IGB) can be quenched entirely, while a finite spectral weight for in-gap feature A (IGA) remains even for the highest possible oxygen partial pressure in the analysis chamber. While both features are comparably intense in the middle row, IGB dominates the spectra taken without O_2 dosing in the bottom row. However, IGA can still be discerned as shoulder at -1.2 eV in the normalized spectra of Fig. S1(f).

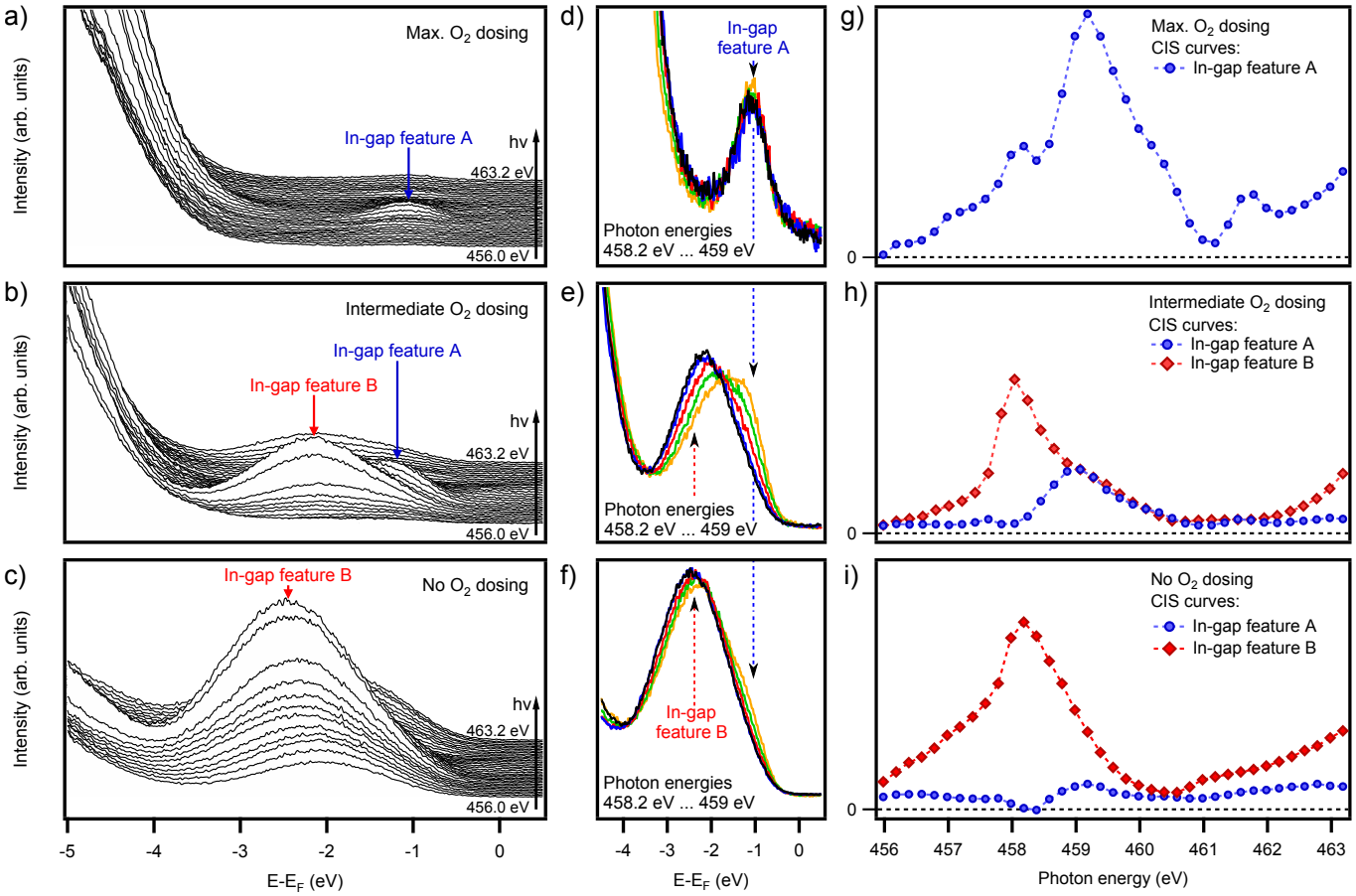

Figure S1. Resonant photoemission spectra upon tuning the photon energy across the Ti *L* edge. (a), (b), (c) Evolution of spectral weight as function of photon energy for three fixed oxygen vacancy concentrations (From top to bottom: Maximal, intermediate, no oxygen dosing). (d), (e), (f) Selected spectra, normalized to the in-gap spectral weight. (g), (h), (i). CIS spectra of the respective spectral features.

SUPPLEMENTAL MATERIAL III. QUASIPARTICLE PHOTON ENERGY DEPENDENCE

Similar to $LaAlO_3/SrTiO_3$, the occupied conduction band states form a small electron pocket at and around the Γ-point in k-space.[6] Hence, visibility in photoemission spectroscopy requires a special experimental geometry. In different geometries, the Γ-region is not probed and when having access to a six-axis manipulator, by choice of the experimenter, one can obtain PES spectra with or without superposition of the quasiparticle. Since in this paper, we focus on the localized in-gap states the spectra in Fig. 2 were obtained without quasiparticle. However, at ADRESS, the evolution of Ti 3d spectral weight as function of photon energy was also measured including the quasiparticle, as shown in Fig. S2. The quasiparticle CIS spectrum from Fig. S3 is extracted from the shown series of spectra. However, since oxygen dosing required the flooding of the analyzer chamber due to the lack of an aluminum capillary pointing at the sample, the tuning of the oxygen stoichiometry could not be performed as precisely as at I09. Hence, the evolution of Ti 3d quasiparticle weight as function of oxygen stoichiometry could not be obtained.

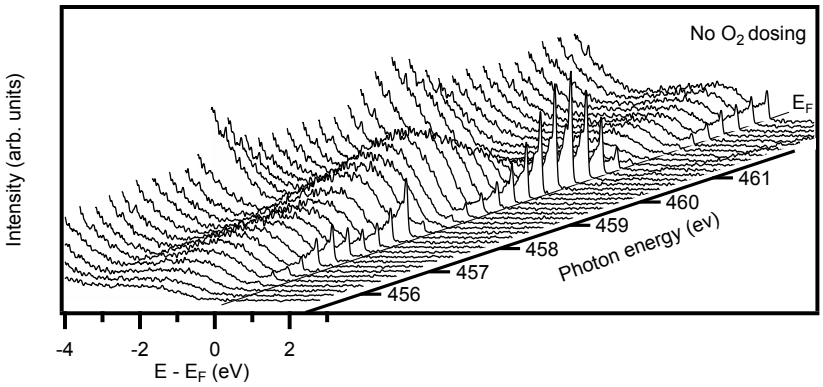

Figure S2. Evolution of Ti 3d spectral weight as function of photon energy, measured at ADRESS.

SUPPLEMENTAL MATERIAL IV. COMPARISON OF γ-$Al_2O_3/SrTiO_3$ AND $LaAlO_3/SrTiO_3$

As summary, the intensity of all in-gap spectral features found in γ-$Al_2O_3/SrTiO_3$ and its all-perovskite counterpart $LaAlO_3/SrTiO_3$ is shown as function of photon energy in Fig. S3. Additionally, x-ray absorption spectra (XAS) of two perovskite compounds with Ti^{4+} ($SrTiO_3$) and Ti^{3+} valence ($LaTiO_3$) are shown. The quasiparticle peaks and the in-gap features at $E = -1.2\,\mathrm{eV}$ in both compounds exhibit qualitatively similar resonance behavior. As explained in the main text, in-gap feature B has a shifted resonance with no equivalent in $LaAlO_3/SrTiO_3$ and is hence characteristic for the spinel/perovskite interface.

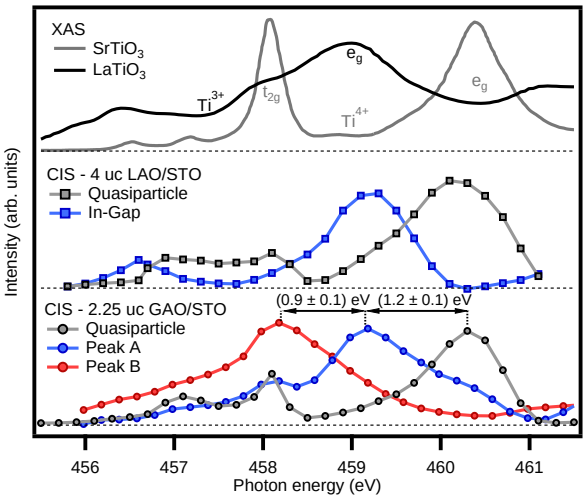

Figure S3. Constant initial state spectra. CIS spectra of all relevant spectral features found in oxygen-deficient $LaAlO_3/SrTiO_3$ and γ-$Al_2O_3/SrTiO_3$ heterostructures. As comparison x-ray absorption spectra (XAS) of two perovskite compounds with Ti^{4+} ($SrTiO_3$) and Ti^{3+} valence ($LaTiO_3$) are shown. Both QP peaks (gray) and the in-gap features found at -1.2 eV (blue) exhibit essentially identical photon energy dependencies in both heterostructures. In contrast, IGB (red) has no equivalent in $LaAlO_3/SrTiO_3$ and is thus characteristic for γ-$Al_2O_3/SrTiO_3$.

SUPPLEMENTAL MATERIAL V. EVOLUTION OF O 2p VALENCE BAND SPECTRAL WEIGHT AS FUNCTION OF PHOTON ENERGY

The finite hybridization between Ti 3d and O 2p states in $SrTiO_3$ is commonly described in a configuration interaction (CI) approach.[7] The charge transfer from O 2p ligand orbitals to Ti 3d orbitals in the initial state can be described as

$$|\Psi\rangle = \alpha \left|3d^0\right\rangle + \beta \left|3d^1\underline{L}^1\right\rangle + \gamma \left|3d^2\underline{L}^2\right\rangle + \dots , \tag{1}$$

where $\underline{L}$ denotes a ligand hole. This hybridization, i.e., essentially the second term in Eq. 1, causes the resonance effect in the valence band observed in Figure S4(a). Since, in case of a heterostructure, a superposition of substrate and film valence band spectral weight is measured, the overall spectral weight observed for $LaAlO_3/SrTiO_3$ and γ-$Al_2O_3/SrTiO_3$ is significantly different. However, as shown in Fig. S4(b), the difference spectra between on- and off-resonance spectra are essentially equal in the valence band region (shaded area), since the resonant spectral weight represents the Ti 3d partial density of states (pDOS) of only the $SrTiO_3$ substrate. The constant initial state (CIS) spectra of the Ti 3d pDOS in comparison to the respective x-ray absorption (XAS) curves are shown in Fig. S4(c). The CIS spectra unambiguously follow the Ti^{4+} XAS spectra, thus evidencing that $\alpha \gg \beta$ in Eq. 1.

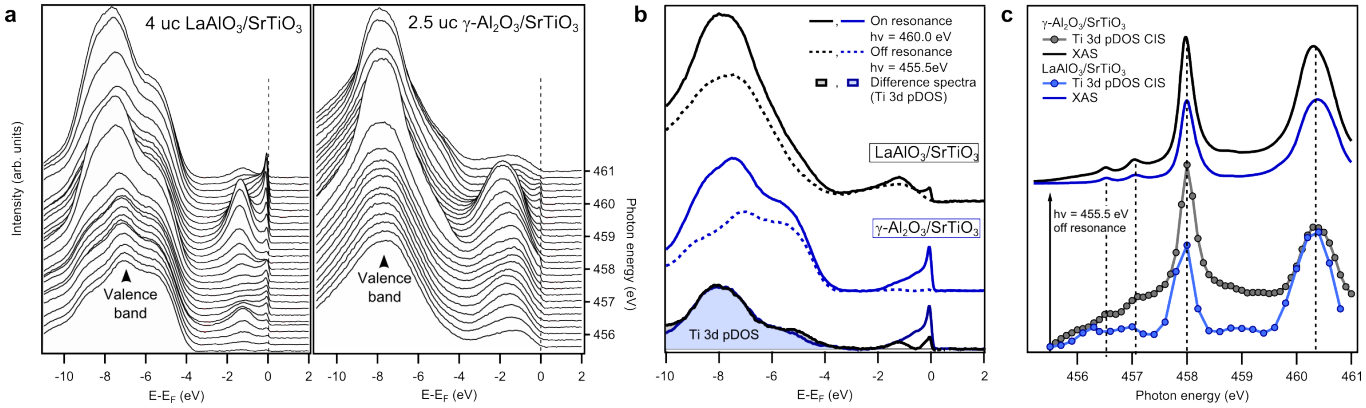

Figure S4. Resonant photoemission spectroscopy of low-energy and valence band states. (a) Evolution of valence band and low-energy spectral weight as function of photon energy in off-stoichiometric, i.e., oxygen-depleted $LaAlO_3/SrTiO_3$ and γ-$Al_2O_3/SrTiO_3$ heterostructures (compare Figure 2(a)). (b) Comparison between off- ($h\nu = 455.5$eV) and on-resonance ($h\nu = 460.0$eV) spectra of $LaAlO_3/SrTiO_3$ and γ-$Al_2O_3/SrTiO_3$ heterostructures. Since we measure a superposition of film and substrate valence band the overall spectral shape differs. However, the on/off-resonance difference spectra, which represent the Ti 3d partial density of states (pDOS) are essentially equal between $E = -10$ eV and -4 eV (shaded area) (c) Constant initial state (CIS) spectra of the Ti 3d partial density of states (shaded area) and x-ray absorption spectra (XAS) for both heterostructures. The CIS spectra unambiguously follow the XAS spectra, since the hybridization between Ti 3d and O 2p is - albeit not zero - very small.

SUPPLEMENTAL MATERIAL VI. DEPTH PROFILING OF OXYGEN-VACANCY INDUCED STATES IGA AND IGB

The intensity ratio curves shown in the inset of Fig. 2(c) (main paper) have been extracted from the measured curves by performing a global fitting scheme. All spectral features, i.e., valence band, in-gap features A and B, and the 2^{nd} order light induced Ti $2p$ core level were modeled as Gaussian peaks with consistent FWHM and binding energy. As shown in Fig. S5, the fit to the experimental data is excellent for all photoelectron emission angles. Note, that the in-gap features A and B exhibit different peak widths of 500 meV and 900 meV, respectively.

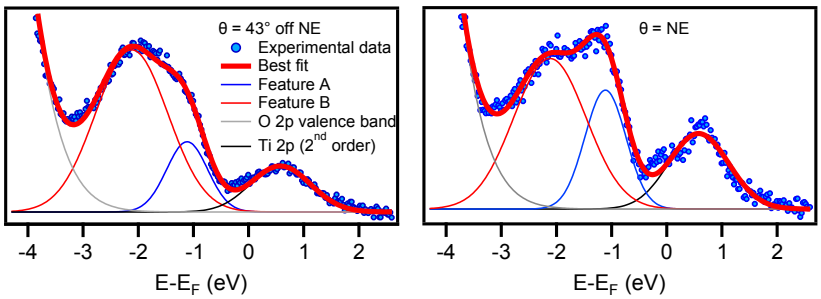

Figure S5. Depth-dependent photoemission spectroscopy. Exemplary fits of the angle-dependent photoemission spectra. A global fitting scheme was adopted to fit all spectra simultaneously using consistent FWHM and binding energies for the respective spectral features.

SUPPLEMENTAL MATERIAL VII. AB INITIO CALCULATIONS: STRUCTURAL MODELS

In this section, we present the structures of the supercells for which the in-gap states were calculated. The γ-$Al_2O_3/SrTiO_3$ interface was simulated by a superlattice (Fig. S6), where 4.5 unit cells of [001]-oriented $SrTiO_3$ were attached to five tetragonal and five octahedral Al layers of the Al_3O_4 spinel structure. One unit cell of γ-Al_2O_3 contains four layers of each type. The in-plane dimensions of the superlattice were chosen to be (2×2) of the standard perovskite unit cell of $SrTiO_3$ to match the oxygen sublattices of the two materials. The real γ-Al_2O_3 adopts a defect-spinel structure, i.e., Al vacancies are present and distributed over the tetragonal and octahedral Al sites.[8–10] In our calculations, we simulated a random distribution of cationic vacancies in the γ-Al_2O_3 part by means of the virtual crystal approximation (VCA)[11] where the charge of each Al cation is shifted by 1/3 towards Mg leading to the nuclear charge Z=12+2/3.

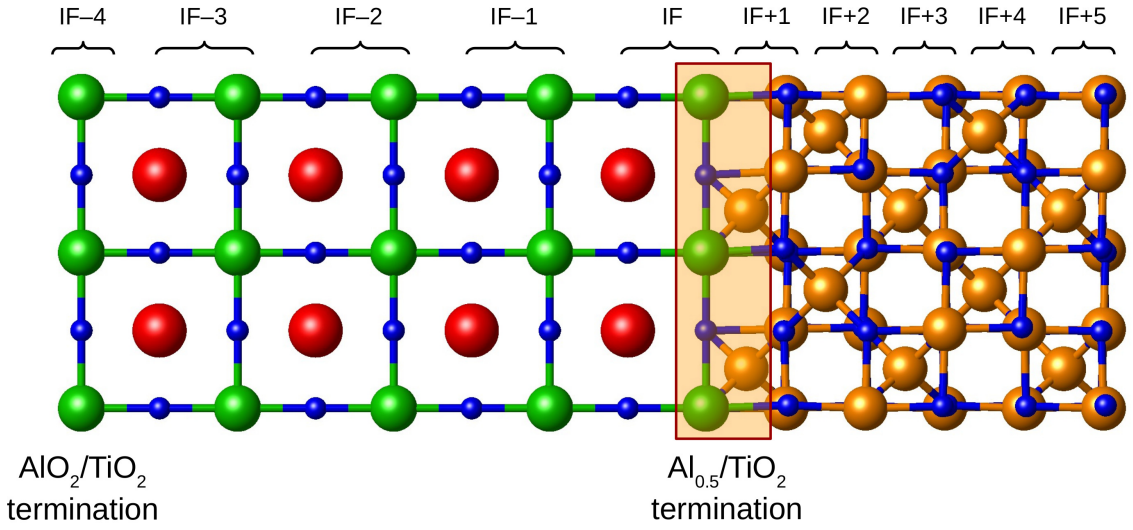

Figure S6. Sketch of the superlattice used to simulate the differently terminated γ-$Al_2O_3/SrTiO_3$ (001) interface. The n-th subsequent $SrTiO_3$ and γ-Al_2O_3 layers are labeled by IF $\pm\, n$ where IF denotes the topmost $SrTiO_3$ unit cell near the electron-doped $Al_{0.5}/TiO_2$ interface (marked with the shaded box). Color code as in Fig. 3(b), main text.

For the comparative analysis with bulk $SrTiO_3$, we built a supercell with $(3 \times 3 \times 3)$ lattice dimensions (see Fig. S7(b)). This cell is large enough to separate the periodic images of a single vacancy and at the same time keeps the computational expense reasonable. On the other hand, it does not allow to start the structural relaxation from the antiferrodistortive (AFD) low-temperature phase of $SrTiO_3$, which would require a much larger $(4 \times 4 \times 4)$ cell for which numerical simulations are hardly feasible. However, since the periodic AFD pattern will be strongly perturbed by the dominating local distortions induced by the vacancy, especially at the high vacancy concentrations studied here, we do not expect qualitative changes when starting the relaxation from the AFD structure. Furthermore, the bonding of the $SrTiO_3$ substrate to the (undistorted) spinel structure of the γ-Al_2O_3 will tend to suppress the AFD pattern at the interface and in its local vicinity, the very region for which we study the formation of oxygen vacancies.

We explicitly included oxygen vacancies in order to take into account not only charge effects but also local symmetry breaking. For this, we constructed different single oxygen vacancy configurations starting from the ideal structure with Al_2/TiO_2 interface termination in Fig. S6. In the bulk $SrTiO_3$ supercell, we considered the case of a single oxygen vacancy. Each structure was internally relaxed using the projector augmented wave basis[12,13] as implemented in VASP code,[14,15] with the in-plane lattice constant fixed at the experimental lattice parameter of 3.905 Å (bulk $SrTiO_3$) in case of the superlattice.[16] For the bulk $SrTiO_3$ supercell, the lattice vectors were additionally optimized. Afterwards, the electronic properties were determined using the full potential local orbital (FPLO) basis set[17] and GGA+U functional[18] (atomic limit double counting) applied to the correlated Ti $3d$ states using the standard values for $U = 5\,\mathrm{eV}$ and $J_\mathrm{H} = 0.64\,\mathrm{eV}$.[19] Real-space maps of the charge density were calculated for the optimized structures using VASP code. Both electronic structure codes (FPLO and VASP) were used for a double check on the density of states and found to yield good agreement. Accordingly, the defect states are very similar in both methods. Due to the different implementations of the GGA+U method in both codes, we used a larger U parameter for the VASP calculations ($U = 8\,\mathrm{eV}$) which is basically equivalent to the standard value used in the all-electron FPLO code (5 eV).

We point out that the tetrahedrally coordinated Al cations at the interface are the key element of the studied

structural interface configuration. While a certain accumulation of Al *vacancies* at the interface may be possible, a recent study[20] has revealed that a finite amount of both Al cations and Al vacancies must be present at the first tetragonal layer of γ-Al_2O_3 in order to make, e.g., a 1 uc film non-polar. According to our model, it is these Al cations which create the symmetry-breaking effect and hence the formation of distinct oxygen vacancies at the perovskite/spinel interface.

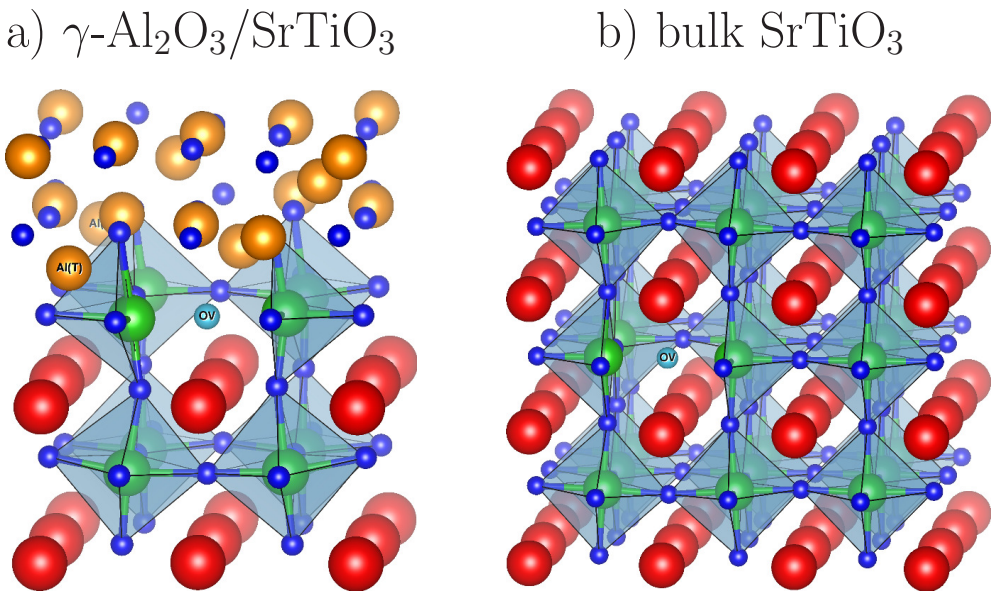

Figure S7. Optimized structure of a) the γ-Al_2O_3/$SrTiO_3$ interface and b) bulk $SrTiO_3$ ($3 \times 3 \times 3$) supercell with a single oxygen vacancy (OV). In panel a), the tetrahedrally coordinated Al cation which neighbors the Ti site near the oxygen vacancy is labeled by Al(T). Color code as in Fig. 3(b), main text.

SUPPLEMENTAL MATERIAL VIII. CRYSTAL FIELD OF DIFFERENT ATOMIC ENVIRONMENTS

In order to support the discussion in the main paper, the crystal field splitting is evaluated for different atomic environments shown in Fig. S8. The crystal-field (CF) splitting was calculated for the five d orbitals of a Ti site which is in the center of an atomic cluster, as shown in Fig. S8. The spatial and angular dependence of the wave functions was modeled using the hydrogen-like atomic orbitals $|nlm\rangle$ constructed from the radial functions and the real harmonics $\tilde{Y}_l^m(\theta,\phi)$:

$$\langle \mathbf{r}|nlm\rangle = R_{nl}(r)\,\tilde{Y}_l^m(\theta,\phi), \tag{2}$$

which build the solution of the Schrödinger equation for a single electron and a nucleus with an effective (unscreened) charge $Z = 22$.
The crystal-field matrix elements are calculated in the basis $\left\{d_{z^2}, d_{x^2-y^2}, d_{xy}, d_{xz}, d_{yz}\right\}$:

$$H^{\mathrm{CF}}_{m_1 m_2} = \langle nlm_1|V_{\mathrm{CF}}(\mathbf{r}) - V_{\mathrm{CF}}(0)|nlm_2\rangle\,, \tag{3}$$

where the potential value at the origin $\mathbf{r} = 0$ is subtracted to allow the comparison between different atomic clusters. In this model, the crystal field itself $V_{\mathrm{CF}}(\mathbf{r})$ includes solely the electrostatic potential contributions from N nearest neighbors of the central Ti cation, each having the charge Q_i and located at the position $\mathbf{r_i}$, while the considered Ti site is placed at $\mathbf{r} = 0$:

$$V_{\mathrm{CF}}(\mathbf{r}) = -\frac{1}{4\pi\varepsilon_0}\sum_{i=1}^{N}\frac{Q_i}{|\mathbf{r}-\mathbf{r_i}|} \tag{4}$$

The minus sign takes into account the negative charge of electrons. For the O, Sr and Al neighbors we assume the nominal charges of -2, $+2$ and $+3$, respectively. Evaluation of the matrix elements (3) is done by means of real-space integration in the cartesian coordinate system. The eigenvalues of the resulting CF matrix represent the CF energy levels, and the corresponding eigenvectors indicate the admixture of each orbital for a given level.

We apply this scheme to study the effect of a single oxygen vacancy on the crystal-field splitting of different atomic environments discussed in the main paper. These environments are simulated by the atomic clusters which include a central Ti site and its nearest and next-nearest neighbors, as shown in Fig. S8. Here, we are interested in the cases of bulk $SrTiO_3$ and two types of the γ-$Al_2O_3/SrTiO_3$ interface, namely, hole-doped AlO_2/TiO_2 and electron-doped $Al_{0.5}/TiO_2$ terminations. For the sake of simplicity, we do not consider the effect of structural relaxation, which is, however, fully included in the density functional theory calculations, and analyze the crystal-field energy levels of the ideal atomic clusters with the three lattice dimensions fixed at the same value 3.905 Å, corresponding to the experimental estimate of the $SrTiO_3$ lattice constant. In each cluster, an oxygen vacancy is created near the Ti site, as indicated by the black arrows in Fig. S8.

The calculated CF energy levels reveal a similarity between the crystal field in bulk $SrTiO_3$ and the hole-doped γ-$Al_2O_3/SrTiO_3$ interface. In contrast to this, the lowest energy orbital for the electron-doped interface has a higher binding energy than for the other two structures. Such behavior can be attributed to the local field created by the tetrahedrally coordinated Al cations which are present near Ti at the $Al_{0.5}/TiO_2$-terminated interface. These cations change the symmetry of the local field and, due to their strongly positive charge, push the electronic orbitals downwards in energy. We note that positively charged Al cations are present at the AlO_2/TiO_2 interface as well, however, they are too distant from Ti to affect the crystal-field splitting in a comparable way. This picture is opposed to the crystal field at the oxygen-deficient $LaAlO_3/SrTiO_3$ interface. There, the crystal field has practically the same structure as in the bulk $SrTiO_3$ with a single oxygen vacancy, which can be explained by the fact that the perturbation induced by both La and Sr neighbors decays with distance as $\sim 1/r^5$, so that the crystal field is determined mostly by the oxygen neighbors.[21]

In general, the calculated binding energy of the in-gap state, marked by the red lines in Fig. S8, is one order of magnitude smaller than the DFT result. This difference can be attributed to the effect of the hybridization and correlations as well as the structural distortions that are fully taken into account in our DFT study, but are absent in the crystal-field analysis. Moreover, the CF calculations in Fig. S8 were done using the unscreened value of the nucleus charge of the central Ti cation. This reduces the average size of the d orbitals and additionally decreases the crystal-field splitting.

To summarize, this simple model of the crystal field facilitates the understanding of the intricate effects observed in the DFT calculations. In agreement with the experimental results in the main manuscript, it demonstrates that the different nature of the atomic environment at the γ-$Al_2O_3/SrTiO_3$ interface can create a new type of the in-gap

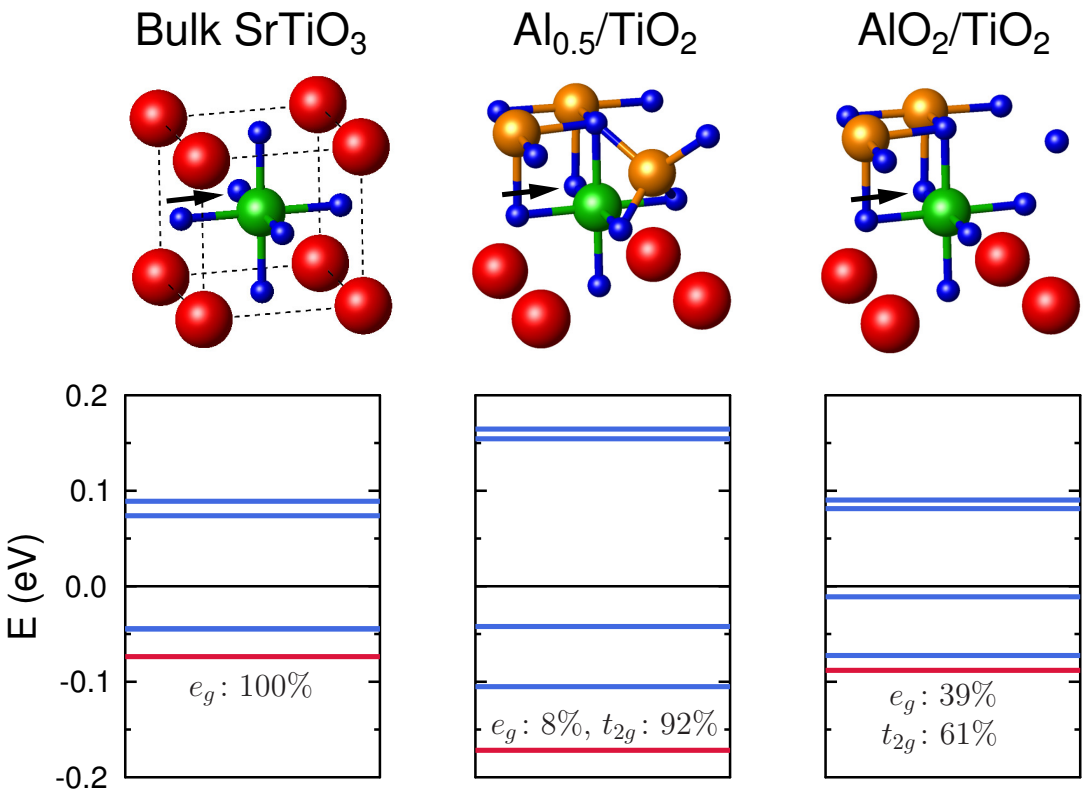

Figure S8. Crystal-field energy levels for different atomic environments: a) bulk $SrTiO_3$, b) electron-doped $Al_{0.5}/TiO_2$-terminated, and c) hole-doped AlO_2/TiO_2-terminated γ-$Al_2O_3/SrTiO_3$ interfaces. The atomic clusters modeling these cases include Sr (red), O (blue) and Al (orange) sites surrounding the central Ti cation (green). In each case, single vacancy is introduced near the central Ti cation on the oxygen site marked with an arrow. The electrostatic potential in the chosen atomic clusters is calculated using $Z = 22$ for Ti and $a = 3.905$ Å for the lattice constant. The lowest d energy level is marked by the red line and its orbital composition is given in terms of the e_g and t_{2g} states.

states with a different orbital character and a higher binding energy, compared to the well-studied $LaAlO_3/SrTiO_3$ and bulk $SrTiO_3$ oxygen-deficient systems.

[1] V. N. Strocov, T. Schmitt, U. Flechsig, T. Schmidt, A. Imhof, Q. Chen, J. Raabe, R. Betemps, D. Zimoch, J. Krempasky, X. Wang, M. Grioni, A. Piazzalunga, and L. Patthey, Journal of Synchrotron Radiation **17**, 631 (2010).
[2] V. N. Strocov, X. Wang, M. Shi, M. Kobayashi, J. Krempasky, C. Hess, T. Schmitt, and L. Patthey, Journal of Synchrotron Radiation **21**, 32 (2013).
[3] P. Scheiderer, F. Pfaff, J. Gabel, M. Kamp, M. Sing, and R. Claessen, Phys. Rev. B **92**, 195422 (2015).
[4] Y. Z. Chen, N. Bovet, F. Trier, D. V. Christensen, F. M. Qu, N. H. Andersen, T. Kasama, W. Zhang, R. Giraud, J. Dufouleur, T. S. Jespersen, J. R. Sun, A. Smith, J. Nygård, L. Lu, B. Büchner, B. G. Shen, S. Linderoth, and N. Pryds, Nat Commun **4**, 1371 (2013).
[5] Y. Z. Chen, N. Bovet, T. Kasama, W. W. Gao, S. Yazdi, C. Ma, N. Pryds, and S. Linderoth, Advanced Materials (2013).
[6] G. Berner, M. Sing, H. Fujiwara, A. Yasui, Y. Saitoh, A. Yamasaki, Y. Nishitani, A. Sekiyama, N. Pavlenko, T. Kopp, C. Richter, J. Mannhart, S. Suga, and R. Claessen, Phys. Rev. Lett. **110**, 247601 (2013).
[7] G. Drera, G. Salvinelli, F. Bondino, E. Magnano, M. Huijben, A. Brinkman, and L. Sangaletti, Phys. Rev. B **90**, 035124 (2014).
[8] R. S. Zhou and R. L. Snyder, Acta Crystallographica B: Structural Science **47**, 617 (1991).
[9] B. Ealet, M. H. Elyakhloufi, E. Gillet, and M. Ricci, Thin Solid Films **250**, 92 (1994).
[10] S.-D. Mo, Y.-N. Xu, and W.-Y. Ching, Journal of the American Ceramic Society **80**, 1193 (1997).
[11] L. Bellaiche and D. Vanderbilt, Phys. Rev. B **61**, 7877 (2000).
[12] P. E. Blöchl, Phys. Rev. B **50**, 17953 (1994).
[13] G. Kresse and D. Joubert, Phys. Rev. B **59**, 1758 (1999).

[14] G. Kresse and J. Furthmüller, Phys. Rev. B **54**, 11169 (1996).
[15] J. Hafner, J. Comput. Chem. **29**, 2044 (2008).
[16] Calculations for the γ-Al_2O_3/$SrTiO_3$ superlattice with lattice parameters scaled up by a few percent to approach the GGA equilibrium value of bulk $SrTiO_3$ resulted in only small shifts of the interfacial in-gap states of the order of 0.1-0.2 eV.
[17] K. Koepernik and H. Eschrig, Phys. Rev. B **59**, 1743 (1999).
[18] A. I. Liechtenstein, V. I. Anisimov, and J. Zaanen, Phys. Rev. B **52**, R5467 (1995).
[19] S. Okamoto, A. J. Millis, and N. A. Spaldin, Phys. Rev. Lett. **97**, 056802 (2006).
[20] D. V. Christensen and A. Smith, Appl. Surf. Sci. **423**, 887 (2017).
[21] E. Pavarini, in *Correlated electrons: from models to materials (Lecture notes of the Autumn School Correlated Electrons 2012)*, Schriften des Forschungszentrums Jülich (2012).